




Influences of Mg content on the microstructures and mechanical properties of cast Al–2Li–2Cu–0.2Zr alloy

Xiaolong Zhang¹, Liang Zhang^{1,2,*} , Guohua Wu^{1,2,*}, Chunchang Shi¹, and Jinshuo Zhang¹

¹National Engineering Research Center of Light Alloy Net Forming and State Key Laboratory of Metal Matrix Composites, School of Materials Science and Engineering, Shanghai Jiao Tong University, Shanghai 200240, People's Republic of China

²Shanghai Innovation Institute for Materials, Shanghai 200444, People's Republic of China

Received: 24 May 2018

Accepted: 16 August 2018

Published online:
20 August 2018

© Springer Science+Business
Media, LLC, part of Springer
Nature 2018

ABSTRACT

This work was undertaken to investigate the influences of Mg content on the microstructure and mechanical properties of cast Al–2Li–2Cu–0.2Zr alloy. The addition of increasing amounts of Mg led to continuous grain refinement of as-cast base alloy accompanied by the increased volume fraction of secondary phases distributed along grain boundaries or interdendritic regions. The tensile test results showed that Mg addition could greatly enhance the mechanical properties of the base alloy after subjected to the solution treatments and artificial ageing. The precipitation behavior and microstructural evolution were also investigated. The addition of Mg would facilitate the nucleation of δ' (Al_3Li) phases after quenching. The presence of Mg was observed to lower the growth rate of δ' and δ' -precipitation-free zones (δ' -PFZs) of the base alloy. Precipitation of θ' (Al_2Cu) phase would be almost suppressed, and S' (Al_2CuMg) phase was consequently introduced due to Mg additions. The precipitation of S' phases was encouraged at the expense of T_1 (Al_2CuLi) phases as the Mg content increased. The increased amount of S' phases tended to coalesce to form coarse laths distributed in uneven manner for alloys with relatively high Mg content (≥ 1 wt%). No improvements in mechanical properties were observed in alloys with heterogeneous distribution of coarse S' laths. The optimal Mg addition in cast Al–2Li–2Cu alloy was 0.5 wt%.

Introduction

The ever-increasing demands for lightweight, high strength, cost-effective and improved stiffness materials lead to successful development of high-

performance aluminum alloys. Weight reduction is considered as the primary approach to fuel savings and payload improvement in the aircraft industry, and lightweight Al–Li alloys are therefore of considerable interest to the airframe manufacturers and

Address correspondence to E-mail: liangzhang08@sjtu.edu.cn; ghwu@sjtu.edu.cn

scholars [1, 2]. Each 1 wt% increment of Li addition to the aluminum alloys (up to 4 wt% Li addition, all compositions are in wt% hereafter unless noted otherwise) could lower the density by about 3% and simultaneously increase the elastic modulus (stiffness) by about 6% [1]. Considering the potentially significant elastic modulus enhancements and weight reduction (10–15%) achieved by replacing the conventional Al alloys, cast Al–Li alloys could meet the increasing demand for high-strength alloys with exceptional properties suitable for weight-critical and stiffness-critical complex structures in aircraft, aerospace and military fields [2, 3]. Casting is also a cost-effective approach to prepare complex structures with weak anisotropy of properties. It is of significance to develop cast Al–Li alloys with specified performance.

A considerable amount of information is available in the literature on the heat treatment, deformation behavior and precipitation strengthening of wrought Al–Li alloys [2–7]. Much less information is available on the alloy composition design, processing and microstructure of cast Al–Li alloys. There exist significant differences on the heat treatment regimes, microstructural evolution and deformation behavior between the wrought and cast alloys since the number density of lattice defects is expected to be much lower in cast alloys. Plastic deformation prior to artificial ageing (T8 temper) in wrought Al–Li–Cu–(X) alloys leads to profound enhancements in strength and ductility over non-deformed materials through the introduction of dense dislocations or other defects [4, 7], which serve as preferential

nucleation sites for the strengthening phases such as T_1 (Al_2CuLi), θ' (Al_2Cu) and S' (Al_2CuMg) phases. Unfortunately, the use of T8 temper is not feasible to cast Al–Li alloys, and thus, the number density of dislocations is intrinsically much lower than that in wrought alloys. Alternatively, certain (minor) alloying additions should be the limited means offering the potential to improve the performance of cast Al–Li alloys. Influences of different (minor) solutes on the overall performances of Al–Li–Cu–X alloys are reviewed based on the literature as follows.

The possible phases encountered in Al–Li–Cu–Mg alloy systems [8–16] are summarized in Table 1. In principle, the (minor) alloying elements could be divided into two types: one serves as the constituent element of the strengthening phases or incorporates into the precipitate phase (including Li, Cu, Mg, Zr), the other facilitates the precipitation of strengthening phases by reducing the interfacial energy (Mg, Ag, Zn) [6, 17] or lowering the solid solubility of the precipitate components in the matrix [18]. Adding Li to Al alloys offers the greatest reduction in density and the modulus enhancement per wt% of any known alloying element, which is primarily derived from the presence of the large volume fraction of coherent, ordered δ' (Al_3Li) phases [8]. The addition of Cu produces Cu-containing strengthening phases involving T_1 , S' and θ' precipitates during artificial ageing while increases the alloy density inevitably [9–13]. The strengthening from Mg addition is due to both solid solution strengthening and precipitation hardening. Mg was reported to lower the solid

Table 1 Phases encountered in Al–Li–Cu–Mg alloy systems

Phases	Crystal structure	Lattice parameters (nm)			Orientation relationship	Ref.
		a	b	c		
δ' (Al_3Li)	$L1_2$	0.405	0.405	0.405	cube–cube	[8]
δ (AlLi)	B_{32} (cubic)	0.637	0.637	0.637	$(100)_\delta // (110)_\alpha$ $(011)_\delta // (111)_\alpha$	[9]
θ' (Al_2Cu)	Tetragonal	0.404	0.404	0.580	$(100)_{\theta'} // (100)_\alpha$ $[001]_{\theta'} // [001]_\alpha$	[10]
T_1 (Al_2CuLi)	Hexagonal	0.4965	0.4965	0.9345	$(0001)T_1 // (111)_\alpha$ $(\bar{1}010)T_1 // (1\bar{1}0)_\alpha$	[11]
S' (Al_2CuMg)	Orthorhombic	0.400	0.923	0.714	$[100]_{S'} // \langle 100 \rangle_\alpha$ $[010]_{S'} // \langle 012 \rangle_\alpha$	[12, 13]
β' (Al_3Zr)	$L1_2$	0.408	0.408	0.408	cube–cube	[14]
T_B ($Al_{7.5}Cu_4Li$)	Cubic	0.611	0.611	0.611	$[001]T_B // [110]_\alpha$ $[001]T_B // [001]_\alpha$	[15]
T_2 (Al_6CuLi_3)	Icosahedral	–	–	–	Unknown	[16]

solubility of Li in α -Al matrix and facilitate the δ' precipitation consequently [18]. Mg (1.848 g/cm³) is also a cost-effective metal element with a lower density than Al (2.7 g/cm³) that can be alloyed with Al. Combined additions of Cu and Mg might result in S' precipitation as well as T_1 and δ' in wrought Al–Li–Cu–Mg alloys [19]. It is well studied that the precipitation kinetics of T_1 phase in wrought alloys will be greatly improved with minor solute additions of Mg, Ag or Zn [6, 17]. However, this microalloying effect might not be so efficient in cast Al–Li–Cu alloys due to the intrinsic lack of dislocations or other defects. Zr addition is effective in retarding recrystallization and reducing grain size in Al–Li alloys, which associated with the precipitation of metastable, coherent β' (Al₃Zr) dispersoids [14]. The specific role of Mn is similar to that of Zr in texture control and retarding recrystallization through the formation of rod-like Al₂₀Cu₂Mn₃ dispersoids [20, 21].

Based on the specific role of the alloying elements and our previously published works [21–23], Al–2Li–2Cu–0.2Zr alloy was applied as the base alloy in this work considering the following aspects. Significant density reduction and modulus improvements were achieved in cast Al–3Li– x Cu–0.2Zr alloys [22, 23] accompanied by a poor tensile ductility. 2% Li addition was applied in an attempt to improve the tensile ductility and fracture toughness to acceptable levels while maintaining the benefit of low density and high modulus. The addition of Cu is essential considering its positive role in strengthening (including solid solution strengthening and precipitation hardening). Combined Cu and Mg addition could improve the tensile strength via forming Cu and Mg-based phases (listed in Table 1) and co-precipitating with the δ' phases. Preliminary work of our group [24] indicated that minor Mg addition to cast Al–2Li–2Cu–0.2Zr alloy would suppress the formation of θ' (Al₂Cu) and encourage the precipitation of S' (Al₂CuMg) phases. S' phase was reported to strongly influence the deformation behavior by promoting cross-slip and inhibiting the planar

deformation [12, 13]. However, the precipitation of S' phase is in competition with T_1 (Al₂CuLi) phase for both available Cu atoms and heterogeneous nucleation sites in the matrix. Addition of increasing amounts of Mg might offer a feasible approach to enhance the precipitation of S' in the absence of a pre-age stretch and enable to further improve the tensile ductility and/or strength of the cast Al–2Li–2Cu–0.2Zr alloy. However, there exists no knowledge of the Mg content or the Cu/Mg ratio on the ageing precipitation behavior, especially the competitive precipitation of T_1 and S' phases in cast Al–Li–Cu–Mg alloys. Systematic studies should be devoted to investigate the specific role of Mg content on the microstructural evolution and especially the competitive precipitation behavior in cast Al–Li–Cu alloys.

The primary aim of this work is therefore to investigate the influences of Mg addition ($x = 0.5, 1.0, 1.5$ and 2.0%) on the microstructures and mechanical properties of cast Al–2Li–2Cu–0.2Zr alloy to develop novel high-strength cast Al–Li alloys with a good tensile ductility. The role of varying Mg contents on the relationships between the microstructural evolution and the tensile properties is discussed in detail. This work also provides a more comprehensive understanding of the precipitate interactions and the competitive precipitation behavior in Al–Li–Cu–(Mg) alloys.

Materials and methods

The cast Al–2Li–2Cu– x Mg–0.2Zr alloys ($x = 0, 0.5, 1.0, 1.5$ and 2.0%) examined in this work were specifically prepared from master alloys of Al–10%Zr, Al–50%Cu and commercial pure Al, Mg and Li. The specifics of the melting procedures have been detailed elsewhere [22, 24]. Chemical analysis was done on as-cast samples using inductively coupled plasma-atomic emission spectroscopy (ICP-AES). The measured chemical compositions for the prepared alloys are listed in Table 2, and they were hereafter

Table 2 Measured chemical composition, density and optimized solutionizing regimes of the Al–2Li–2Cu– x Mg–0.2Zr alloys in this work

Alloy	Li	Cu	Mg	Zr	Fe	Al	Density	Solutionizing regimes
Base	1.96	1.89	–	0.17	0.10	Bal.	2.576	460 °C × 32 h + 520 °C × 24 h
0.5 Mg	1.98	1.93	0.45	0.18	0.11	Bal.	2.574	
1.0 Mg	2.03	2.09	0.91	0.15	0.13	Bal.	2.570	460 °C × 32 h + 530 °C × 32 h
1.5 Mg	1.70	1.90	1.39	0.15	0.12	Bal.	2.568	460 °C × 32 h + 540 °C × 24 h
2 Mg	1.93	1.93	1.95	0.15	0.11	Bal.	2.562	–

denoted by the base, 0.5 Mg, 1 Mg, 1.5 Mg and 2 Mg alloy, respectively. The density of each alloy (g/cm^3) was measured using standard Archimedes method, and the results are listed in Table 2. The as-cast samples were subjected to the differential scanning calorimetry (DSC, NETZSCH, STA 449F3) tests at a constant heating rate of $10\text{ }^\circ\text{C}/\text{min}$ to determine the proper temperature for solution treatment. The as-cast prepared alloys were processed with the optimized two-step solutionizing regimes listed in Table 2, which were determined by combining metallographic examinations and DSC measurements. Samples from all alloys were immediately quenched in water after solution treatment (referred to as as-quenched state) and subsequently aged at $175\text{ }^\circ\text{C}$ for various time periods ranging from 0 h to 1200 h in a vigorously stirred silicon oil bath.

Phase analysis was carried out by X-ray diffraction (XRD, Rigaku Ultima IV) on polished samples scanning over the 2θ interval 10° – 90° with an angular velocity of $4\text{ deg}/\text{min}$. Samples of $10\text{ mm} \times 10\text{ mm} \times 5\text{ mm}$ in size cut from the same position of the as-cast and as-quenched ingots were subjected to conventional mechanical polishing followed by etching with the Keller's reagent for 20 s prior to optical (OM, LEICA MEF4 M) and scanning electron microscopy (SEM, Phenom XL) observations. The sample preparation procedures for OM and SEM observations have been detailed elsewhere [24]. Macro-Vickers hardness tests were carried out on polished samples using a load of 5 kg and a dwell time of 15 s. Every result is the average of six tests.

Tensile tests of sheet specimens were tested at room temperature utilizing Zwick/Roell Z100 testing machine with a strain rate of $1.0 \times 10^{-3}/\text{s}$. Specimens were sectioned from untested tensile samples for transmission electron microscopy (TEM) observations. Thin foils were prepared by electropolishing 3-mm-diameter disks punched from selected specimens mechanically ground to approximate $100\text{ }\mu\text{m}$. The disks were twin-jet electropolished using a TenuPol-5 twin-jet electropolisher operating at 30 V. A solution of 4% perchloric acid and 96% ethanol cooled to approximately $-30 \sim -40\text{ }^\circ\text{C}$ was applied as the electrolyte. All samples were examined in a JEOL 2100 TEM apparatus operating at 200 kV.

Results and discussion

Effect of Mg Content on the As-cast microstructures

Figure 1a presents the XRD patterns of as-cast Al-2Li-2Cu-0.2Zr alloys with different Mg additions. It can be seen that peaks from α -Al, δ' (Al_3Li) and T_1 (Al_2CuLi) phases are observed in the spectrum of the as-cast base alloy, while extra diffraction peaks from Al_2Cu , Al_2CuMg and T_2 (Al_6CuLi_3) phases are well-defined in the as-cast Mg-added alloys. The T_2 and δ (AlLi) phases were not determined in our previous work [24] possibly ascribed to the relatively larger angular scanning velocity ($10\text{ deg}/\text{min}$) rather than the $4\text{ deg}/\text{min}$ used in this study. In the spectrum of as-cast 1 Mg, 1.5 Mg and 2 Mg alloys shown in

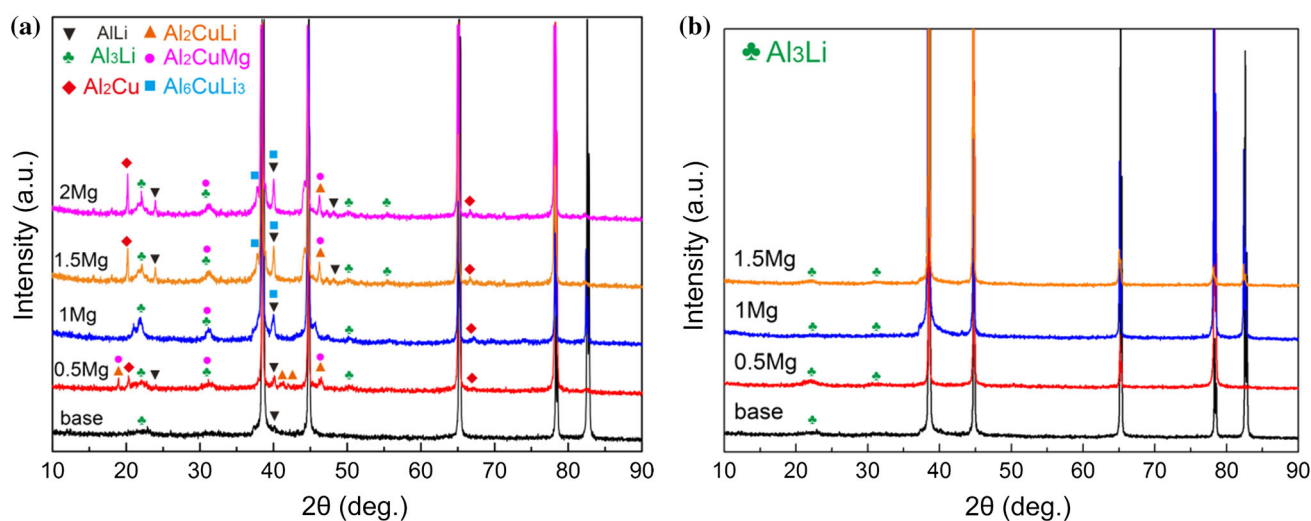


Figure 1 XRD patterns of Al-2Li-2Cu- x Mg-0.2Zr alloys in: **a** as-cast and **b** as-quenched states.

Fig. 1a, the characteristic diffraction peaks associated with T_2 phase show higher intensities than those in the 0.5 Mg alloy. Mukhopadhyay et al. [25] reported that Mg could incorporate into T_2 phase, presented in the form of $Al_6Cu(Li, Mg)_3$, and the plate-like T_2 phase would be the major coarse grain boundary precipitates in the as-cast low Mg high Cu 8090 alloys. The authors speculate that the higher intensities associated with the T_2 phase should be primarily attributed to the increasing amounts of Mg additions. Table 1 lists all the symbol, lattice parameters and orientation relationships of the possible phases encountered in Al–Li–Cu–Mg alloy systems [8–16].

Previous studies by Fridlyander et al. [26] provided indications of the coexistence of T_1 , Al_2Cu , $AlLi$, Al_2CuMg , Al_2MgLi , T_2 and T_B ($Al_{7.5}Cu_4Li$) phases in quaternary Al–Li–Cu–Mg systems. However, no diffraction peaks related to Al_2MgLi and T_B phases are presented in Fig. 1a, possibly attributed to their limited presence.

Figure 2 shows the typical comparative micrographs of as-cast Al–2Li–2Cu– x Mg–0.2Zr alloys. The microstructure of the as-cast base alloy, as illustrated in Fig. 2a, consists of dendritic α -Al grains and coarse secondary phases distributed along the grain boundaries or interdendritic regions. The amount of

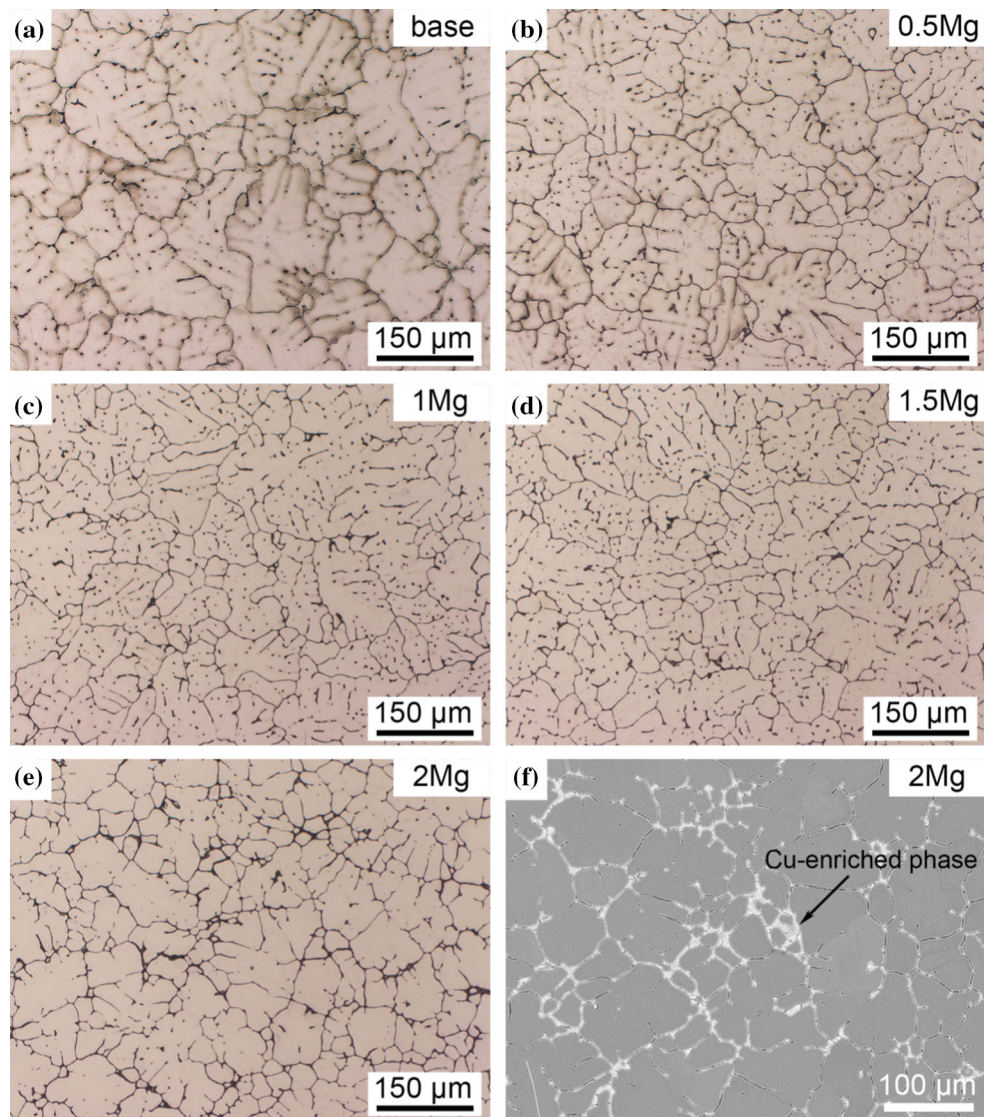


Figure 2 Microstructures of as-cast Al–2Li–2Cu–0.2Zr alloys with different Mg additions, indicating the gradually reduced dendrite arm spacing due to the increase in Mg content: **a** base

alloy; **b** 0.5 Mg alloy; **c** 1 Mg alloy; **d** 1.5 Mg alloy; **e** 2 Mg alloy; and **f** SEM backscattered micrograph of as-cast 2 Mg alloy.

secondary phases is observed to increase with the increase in Mg content. With the increase in Mg content from 0 to 2%, gradual reduction in dendrite arm spacing (DAS) can be observed as well as an accompanying change from dendritic to a combination of dendritic and equiaxed grains. The microstructure of as-cast 2Mg alloy is characterized by the combination of fine equiaxed α -Al grains and coarse cellular α -Al grains (presented in Fig. 2e, f). The grain refinement observed in this work is in agreement with the observations obtained by Wang et al. [27]. The increased degree of grain refinement with the increasing addition of Mg is primarily ascribed to the contribution of solute segregation (constitutional undercoolings).

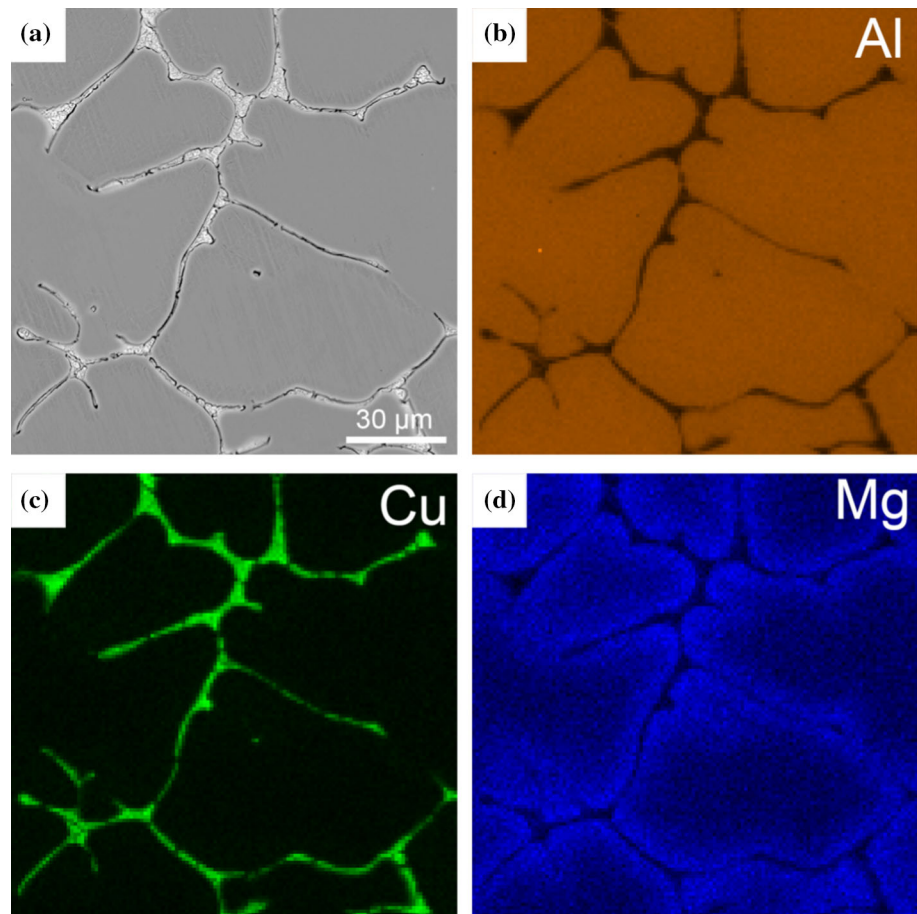
Figure 3 displays the SEM backscattered micrograph and the corresponding element distributions acquired by EDS of as-cast 1.5 Mg alloy. For the purpose of brevity, similar analysis results of as-cast base alloy and other Mg-added alloys are not shown. The distribution of Li could not be obtained because of its low atomic number. Element Cu is significantly

enriched in the coarse secondary phases distributed along the grain boundaries or interdendritic regions. As indicated in Fig. 3c and d, slight segregation tendency of Mg is observed in the vicinity of Cu-rich phases. Unfortunately, Cu-rich secondary phases such as Al_2Cu , Al_2CuLi , Al_2CuMg and Al_6CuLi_3 are failed to be distinguished since element Li could not be detected. It is evidenced that element Cu exhibits the highest severity of segregation in the matrix during solidification, probably ascribed to the different solute partitioning coefficients of Mg, Cu and Li in binary Al-X (X indicates Cu, Li, and Mg) systems [28].

Effect of Mg content on the solution heat treatment

The DSC results of the as-cast Al-2Li-2Cu- x Mg-0.2Zr alloys are presented in Fig. 4. It can be seen that the common endothermic peak sited at 525 ± 3 °C occurs in all as-cast studied alloys, which is attributed to the dissolution of Cu-rich secondary phases

Figure 3 SEM backscattered micrograph and elements map-scanning of as-cast 1.5 Mg alloy: **a** SEM image; **b** Al distribution; **c** Cu distribution; **d** Mg distribution.



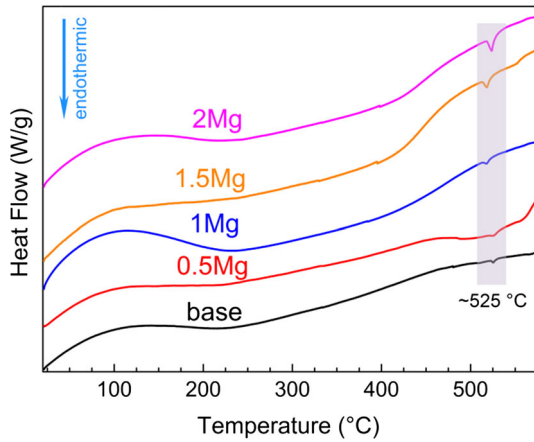


Figure 4 DSC results of the as-cast Al-2Li-2Cu-*x*Mg-0.2Zr alloys.

based on our previous works [22, 24]. Cu addition might form Al₂Cu, T₁ and T₂ phases in the presence of Li. Additions of Cu and Mg in combination could also lead to the formation of Al₂CuMg based on the XRD results shown in Fig. 1a. However, no detection of several separate endothermic peaks is obtained associated with these secondary phases as reported by Elgallad et al. [29], possibly attributed to their respective low-volume fractions. Furthermore, with the increase in Mg addition, the volume fraction of Cu-rich phases is significantly increased, resulting in the higher difficulty to maximize the dissolution of secondary phases. Based on the different melting points of these phases, two-step solution treatments are needed and 460 °C is applied as the safe temperature of the first stage. Furthermore, a suitable higher temperature for second-stage solution treatment is essential to ensure most Cu-rich secondary phases can be dissolved in the α-Al matrix without the occurrence of overburnt microstructures.

In principle, the solvus temperature represents the temperature capable of maximizing the dissolution of secondary phases, which should be lower than the solidus temperature. Previous works by Dorward et al. [30] provide references for the evaluation of solvus and solidus temperature in quaternary Al-Li-Cu-Mg alloys, which could be interpreted as the following mathematical representations (in °C):

$$T(\text{solvus}) = 284 + 67.0(\%Li) + 34.6(\%Cu) + 36.5(\%Mg) \quad (1)$$

$$T(\text{solidus}) = 730 - 24.5(\%Li) - 33.2(\%Cu) - 49.0(\%Mg) + 10.0(\%Mg)^2 \quad (2)$$

The solution temperature applied should be in the vicinity of the solvus temperature and not exceed the solidus temperature.

Combined the solvus temperatures with the practical metallographic observations, the respective two-step solutionizing regimes for the studied alloys are successfully optimized except for the 2 Mg alloy (listed in Table 2). Figure 5 displays the representative optical micrographs of the as-quenched Al-2Li-2Cu-*x*Mg-0.2Zr alloys. The majority of the secondary phases are dissolved into the α-Al matrix for the base, 0.5 Mg, 1 Mg and 1.5 Mg alloys, which is consistent with the XRD results of as-quenched samples presented in Fig. 1b. The second-stage solution temperature is increased with the increasing Mg content in order to maximize the dissolution of the Cu-rich phases, of which the volume fraction is higher in alloy with higher Mg additions. Residual secondary phases are observed in 2 Mg alloy as shown in Fig. 5e, and they mainly gathered at the grain boundaries. The solution temperature of 540 °C is not capable of sufficiently dissolving the secondary phases for 2 Mg alloy even though prolonging the second-stage solutionizing time up to 40 h. A higher second-stage solution temperature (550 °C) applied leads to the occurrence of overburnt microstructure observed in 2 Mg alloy (illustrated in Fig. 5f). Thus, improving the second-stage solution temperature is not applicable. The addition of Mg in cast Al-2Li-2Cu-0.2Zr alloy should not exceed 1.5%.

Effect of Mg content on the mechanical properties

At an ageing temperature of 175 °C, Fig. 6 shows the macro-Vickers hardness as a function of ageing time for Al-2Li-2Cu-*x*Mg-0.2Zr alloys (*x* = 0, 0.5, 1 and 1.5). The hardness of as-quenched samples is observed to increase in steps with the increased Mg content, which should be largely attributed to the enhanced precipitation of δ' phases. Besides, the solid solution strengthening of increasing amounts of Mg also contributes to the improved hardness (strength) of as-quenched samples. All the alloys possess a strong ageing hardening response, while the highest peak value of 184 HV is obtained in the 0.5 Mg alloy. The addition of Mg will accelerate the ageing hardening response, and the time taken to reach the peak

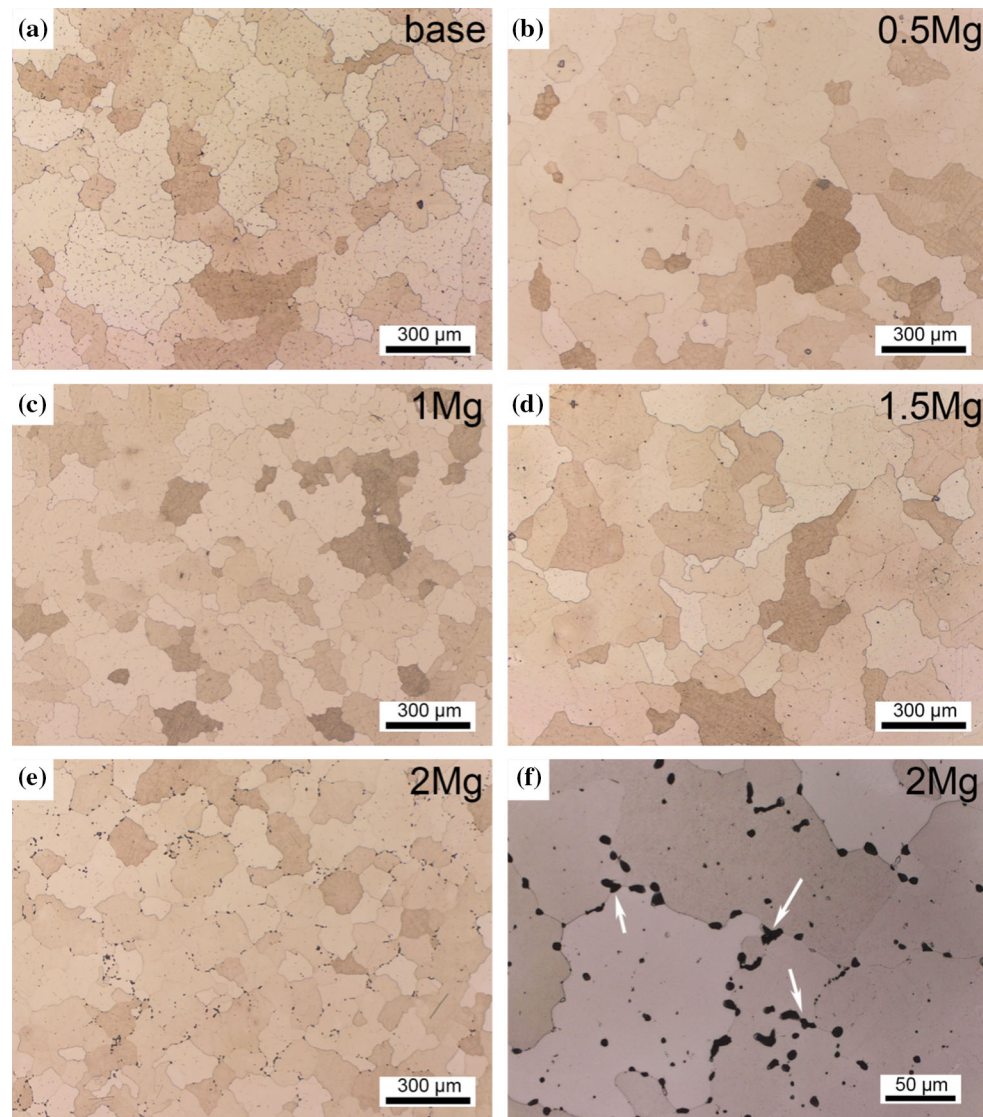


Figure 5 Microstructures of the Al-2Li-2Cu- x Mg-0.2Zr alloys subjected to different solution treatments: **a** and **b** the base alloy and 0.5 Mg alloy solution treated at 460 °C \times 32 h + 520 °C \times 24 h, respectively; **c** the 1 Mg alloy solution treated at 460 °C \times 32 h + 530 °C \times 32 h; **d** the 1.5 Mg alloy solution

treated at 460 °C \times 32 h + 540 °C \times 24 h; **e** the 2 Mg alloy solution treated at 460 °C \times 32 h + 540 °C \times 40 h; and **f** the 2 Mg alloy solution treated at 460 °C \times 32 h + 550 °C \times 24 h, showing typical overburnt microstructures distributed along grain boundaries (arrowed).

hardness for the base alloy (161 HV) is reduced from about 128 h to about 32 h in 0.5 Mg alloy.

Figure 7 presents the mechanical properties involving yield strength (YS), ultimate tensile strength (UTS), elongation (EL) and representative engineering stress-strain curves of the studied alloys under different states. The as-quenched 2 Mg alloy subjected to the insufficient solution treatment exhibits much lower strength (UTS= 306 MPa, YS= 196 MPa) and ductility (EL= 6.0%) as shown in Fig. 7d, which is primarily ascribed to the presence of large

amount of residual Cu-rich secondary phases. Valid mechanical property results for aged 2 Mg alloy are not obtained due to the premature fracture. It is noteworthy that the addition of Mg greatly improves the YS and UTS of the as-quenched base alloy over 100 MPa (presented in Fig. 7a, b), indicating that Mg could serve as a potent strengthener for cast Al-Li-Cu alloys and the addition should not exceed 1.5% in this work.

As ageing proceeds, the YS and UTS will strongly increase with the prolonged ageing times for all

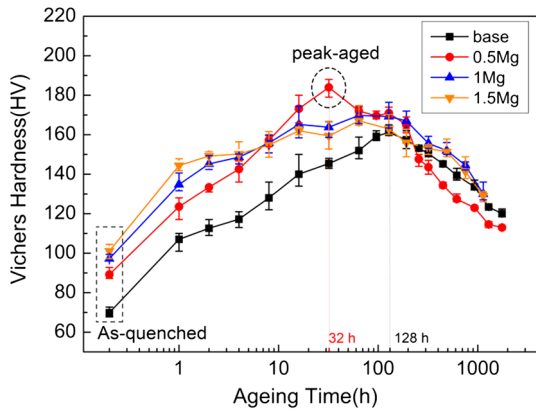
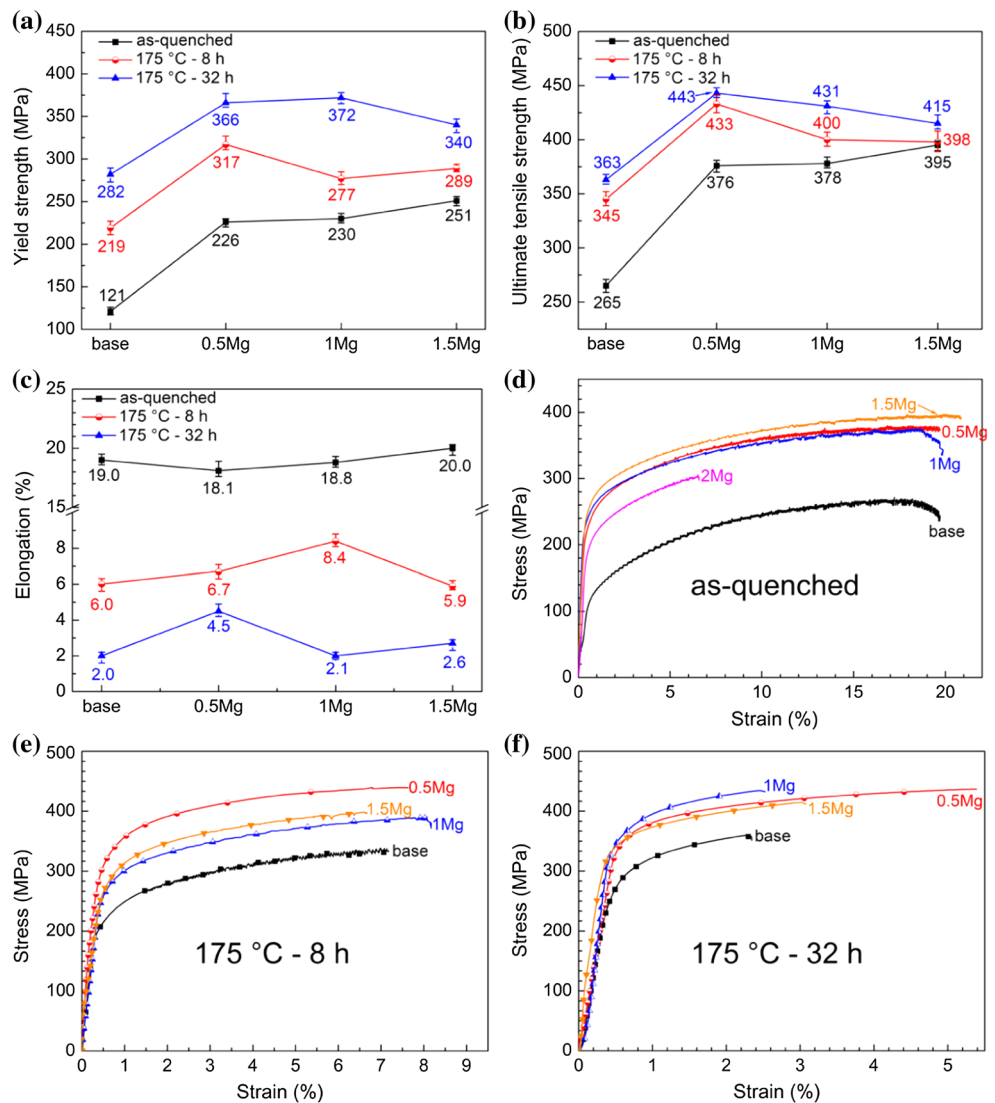


Figure 6 Macro-Vickers hardness as a function of artificial ageing time for the Al-2Li-2Cu-xMg-0.2Zr alloys aged at 175 °C.

alloys, accompanied by a significantly monotonic decrease in tensile ductility. Minor Mg addition (0.5%) is revealed to strongly improve the strength of Al-2Li-2Cu-0.2Zr alloy as illustrated in Fig. 7a and b. There exists a drop in strength and/or ductility during artificial ageing when the Mg content increases from 0.5% to 1.5%. The best combinations of strength (UTS= 443 MPa, YS= 366 MPa) and ductility (EL= 4.5%) are obtained in the 0.5 Mg alloy aged for 32 h at 175 °C. The YS and/or UTS for the 1 Mg and 1.5 Mg alloys is lower than that for the 0.5 Mg alloy concomitant with a significant decrease in ductility after aged for 32 h. The influences of different Mg contents on the development of mechanical per-

Figure 7 Mechanical properties and typical engineering stress–strain curves of the Al-2Li-2Cu-xMg-0.2Zr alloys: **a** the yield strength (YS) of the studied alloys under different states, including as-quenched and aged at 175 °C for 8 h and 32 h; **b** the ultimate tensile strength (UTS) of the studied alloys under different states; **c** the elongation (EL) variations of the studied alloys under different states; **d**, **e** and **f** typical engineering stress–strain curves of the studied alloys under different states involving as-quenched, artificial ageing for 8 h and 32 h at 175 °C, respectively.



mances and ageing precipitation behavior will be discussed in the following section.

Effect of Mg content on the ageing precipitation behavior

To gain a better understanding of the relationships between the microstructural evolution and the mechanical properties, samples of Al–2Li–2Cu– x Mg–0.2Zr alloys ($x = 0, 0.5, 1$ and 1.5) were selected for TEM observations under different heat treatment conditions, including artificial ageing at $175\text{ }^{\circ}\text{C}$ for 0 h (as-quenched), 8 h (under-aged, UA), 32 h (peak-aged 0.5 Mg alloy, PA), 128 h (peak-aged base alloy) and 600 h (over-aged, OA).

The as-quenched microstructure

Heterogeneous distribution of Al_3Zr dispersoids is revealed in the as-quenched base alloy as exemplified in Fig. 8a. The distribution of these coherent Al_3Zr dispersoids is essentially similar in all studied alloys, and they could offer additional nucleation sites for δ' particles [31]. The as-quenched 1 Mg alloy is characterized by predominantly coherent, extremely fine, homogeneous distribution of δ' as exemplified in Fig. 8b. Similar δ' -centered dark-field (δ' CDF) images of other alloys are not shown for the purpose of brevity. Water quenching is inadequate to prevent nucleation of the ordered δ' phase as evidenced by the homogeneous distribution of δ' particles shown in Fig. 8b.

As illustrated in Fig. 7a, the addition of Mg would greatly improve the YS of the base alloy from about 121 MPa to about 251 MPa in the 1.5 Mg alloy, which attracts our interest. In order to basically eliminate the influence of natural ageing (NA) hardening, the tensile tests were conducted as soon as possible after water quenching. The as-quenched samples were also subjected to NA process at room temperature for 24 h, and the measured results of as-quenched samples are in fully consistent with those directly tested after quenching. Natural ageing hardening provides negligible contribution to the strength enhancements in this work.

The main reason for the remarkable strength enhancements, we speculate, is that the overall precipitation kinetics of δ' is strongly enhanced in the presence of Mg. On the one hand, precipitation of δ' will be favored since the addition of Mg will increase the misfit of $\delta'/\alpha\text{-Al}$ matrix and consequently lower the solid solubility of Li in matrix [18]. On the other hand, the presence of Mg atoms was reported to improve the equilibrium vacancy concentration during solution treatment and retain the vacancies through quenching operation [32]. Moreover, higher vacancy concentrations would be obtained due to the higher second-stage solution temperature applied in the alloy with higher Mg content [33]. The increased concentration of vacancies trapped in the matrix would result in the augmented diffusion coefficient of Li in matrix, thus enhancing the overall δ' precipitation kinetics [32, 34]. Baumann et al. [34] provided

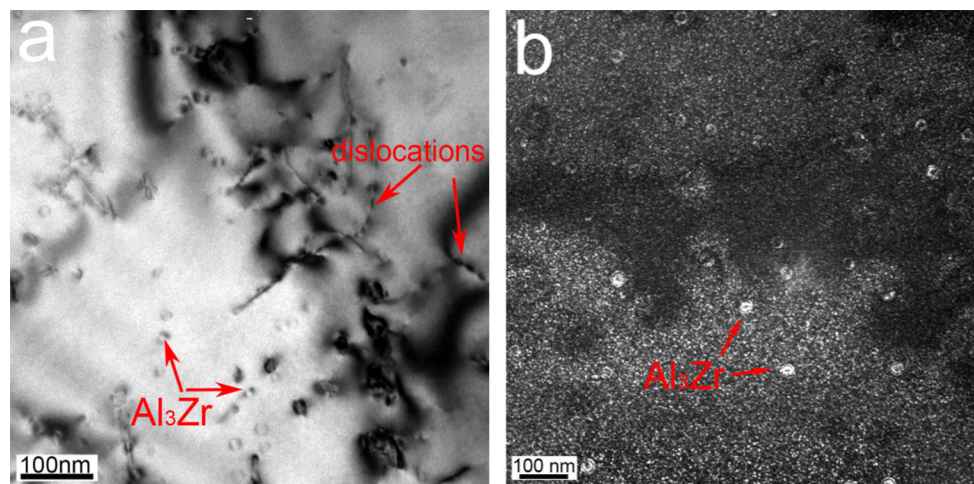


Figure 8 TEM images of the as-quenched studied alloys showing: **a** heterogeneous distribution of coherent Al_3Zr dispersoids and presence of dislocations in the base alloy; **b** δ' centered dark-

field (δ' CDF) image of as-quenched 1 Mg alloy, recorded using 110 superlattice reflections in the $[011]_{\alpha}$ zone axis, indicating homogeneous distribution of very fine δ' particles.

a rough approximation to the δ' nucleation rate in the following equation:

$$J_{\text{homo}}^* = D \cdot N_{\text{homo}} \cdot \exp(-\Delta G_{\text{homo}}^*/kT) \tag{3}$$

where J_{homo}^* is the nucleation rate, D is the diffusion coefficient of Li, N_{homo} is the number of potential nucleation sites, ΔG_{homo}^* is the free energy barrier to homogeneous nucleation of δ' and kT is the thermal energy. The δ' nucleation rate should be improved as the diffusion coefficient D increases with improved excess vacancies and addition of Mg leads to a reduction in ΔG_{homo}^* . It can be expected that the volume fraction of δ' is higher in the as-quenched Mg-added alloys. The increase in critical resolved shear stress (CRSS) $\Delta\tau_{\text{CRSS}}$ due to the ordered δ' particles can be evaluated using the following equation given by [35]:

$$\Delta\tau_{\text{CRSS}} = 0.28 \gamma^{3/2} G^{-1/2} b^{-2} r_0^{1/2} f^{1/2} \tag{4}$$

where γ is the δ' phase antiphase boundary energy ($\gamma = 0.18 \text{ J m}^{-2}$), G is the shear modulus of the matrix ($G = 29.7 \text{ GPa}$) [34], b is the Burgers vector ($b = \frac{a}{2} \langle 110 \rangle = 0.286 \text{ nm}$), r_0 is the average radius and f is the volume fraction of δ' particles. Unfortunately, the precise data of r_0 and f for each alloy are not available due to the extremely fine δ' distribution in as-quenched alloys. Besides, the solid solution strengthening effect associated with Mg atoms also contributes to the strength improvements of as-quenched studied alloys.

The UA stage microstructures due to Mg variations

Previously published work of our group investigated the microstructural evolution of 0.5 Mg alloy in detail [24]. In this work, we will mainly concentrate on the microstructural evolution of the base alloy in the presence of different Mg additions. Figure 9 shows comparative bright-field (BF) and δ' CDF images of the base and 0.5 Mg alloys aged for 8 h at 175 °C. The spherical δ' particles in both aged alloys are significantly larger in size and fewer in number than those in the as-quenched samples. Continued nucleation and subsequent growth of the ordered δ' particles take place in both alloys, accompanied by the formation of core/shell composite $\text{Al}_3(\text{Li}, \text{Zr})$ precipitates (or denoted by β'/δ') as illustrated in Fig. 9b and d. The $\text{Al}_3\text{Zr}/\alpha\text{-Al}$ matrix interface was reported to serve as the preferential nucleation sites for the δ' due

to the reduction in both surface and strain energy [31, 36]. Heterogeneous precipitation of δ' on preexisting Al_3Zr particles will relieve the misfit strain between δ' and $\alpha\text{-Al}$ matrix, thereby reducing its nucleation barrier. The 1 Mg and 1.5 Mg alloys aged for 8 h undergo a similar microstructural evolution as illustrated in Fig. 10b and d. Moreover, composite $\text{Al}_3(\text{Li}, \text{Zr})$ precipitates with faceted and/or rod-shaped morphology are occasionally observed as exemplified in Figs. 9b and 10b. They arise as a result of heterogeneous nucleation of δ' on the preexisting faceted or rod-shaped Al_3Zr particles. The formation of Al_3Zr with faceted or rod-shaped morphology is mainly attributed to the repeated precipitation on climbing dislocations associated with the interactions of spherical Al_3Zr with the mobile dislocations and/or grain boundaries [37, 38].

The additions of increasing amounts of Mg exert significant influence on the ageing precipitation behavior, where an evident altering in precipitate types can be observed as well as an accompanying variation of the predominant Cu-containing strengthening phases. The Cu-containing θ' , S' and T_1 phases could be identified based on their different habit planes and orientation relationships listed in Table 1 [10–13], and the detailed illustrations to distinguish these phases are available in the appendix of this work.

Figure 9a is a BF image ($\mathbf{B} = [\bar{1}12]$) of the base alloy showing the distribution of few T_1 and θ' phases. In this foil direction, only the T_1 variant lying on $(1\bar{1}1)$ plane is viewed edge-on, which is parallel to the electron beam. These edge-on T_1 plates appear as thin lines (arrowed T_1 in Fig. 9a), while other T_1 variants should be viewed face-on (T_1 variant orientated with broad face inclined to the beam direction, arrowed A in Fig. 9a). It is noticeable that the addition of Mg would suppress the formation of θ' (Al_2Cu) and encourage the precipitation of S' (Al_2CuMg) phases. No evidence for the formation of θ' phases is obtained in the 0.5 Mg alloy, while the additional S' phases with lath-shaped morphology are observed as shown in Fig. 9c. Owing to the unique orientation relationship (OR) with the matrix ($[100]S' // \langle 100 \rangle_\alpha$, $[010]S' // \langle 012 \rangle_\alpha$) [13], S' phase is expected to improve toughness and reduce the anisotropy of properties by inhibiting the development of planar slip [39].

A dense, homogeneous S' distribution is capable of improving the tensile ductility of Al–Cu–Li–Mg

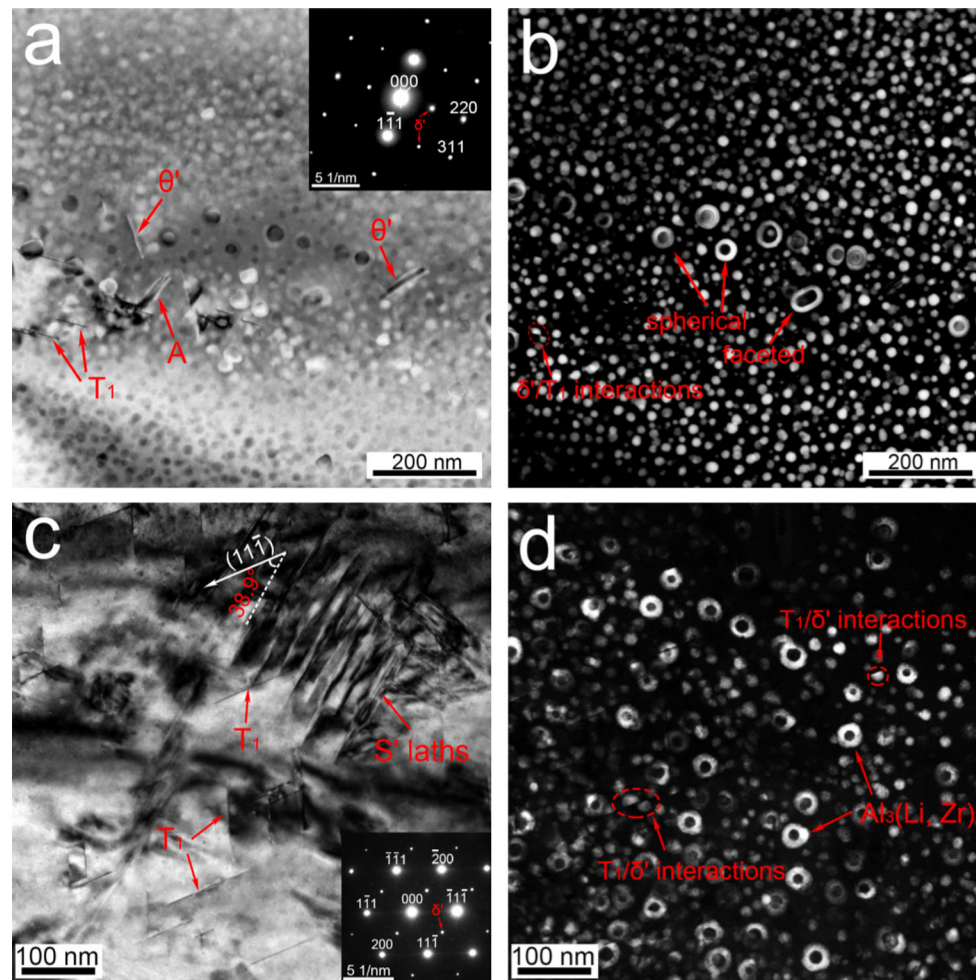


Figure 9 TEM images of the base and 0.5 Mg alloys aged at 175 °C for 8 h: **a** the bright-field (BF) image combined with SAED pattern ($B = [\bar{1}12]$, inset) of the base alloy showing the distribution of few T_1 and θ' precipitates; **b** the corresponding δ' CDF image of the base alloy indicating the homogeneous δ' distribution accompanied by a few $Al_3(Li, Zr)$ composite precipitates with spherical

and basically faceted morphology; **c** BF image of 0.5 Mg alloy evidencing the coexistence of plate-like T_1 and lath-shaped S' phases ($B = [011]$, inset); **d** δ' CDF image of 0.5 Mg alloy showing the dense distribution of δ' and $Al_3(Li, Zr)$ precipitates and the typical T_1/δ' interactions.

alloys [39]. The present work aims to promote the homogeneous precipitation of S' phases via optimizing the Mg content and thereby improve the toughness while retaining or enhancing the required high strength. The S' and T_1 phases will compete for the available Cu atoms and heterogeneous nucleation sites in the matrix [19]. With the increase in Mg content, S' precipitation is observed to be promoted at the expense of T_1 phases as evidenced by comparing Figs. 9c, 10a and 10c. The retarded precipitation of T_1 phases observed in 1 Mg and 1.5 Mg alloy (shown in Fig. 10a, c) results in the reduction in YS and UTS illustrated in Fig. 7a and b since T_1 plates are

reported to be the precipitates offering the maximum strengthening effect in Al–Cu–Li–(Mg) alloys [40]. The distribution of S' tends to exhibit in a sparse and uneven manner as the Mg content exceeds 1% (presented in Fig. 10c), which provides little contribution to the enhancement of ductility and strength. Gregson and Flower [39] also confirmed that no improvement in properties was observed in Al–Li–Cu–Mg alloy with uneven distribution of coarse S' phases. In addition, two types of precipitate interactions are revealed. One is the typical T_1/δ' interactions, as illustrated in Fig. 9d (indicated by dotted oval), that the T_1 could cut/grow through the δ'

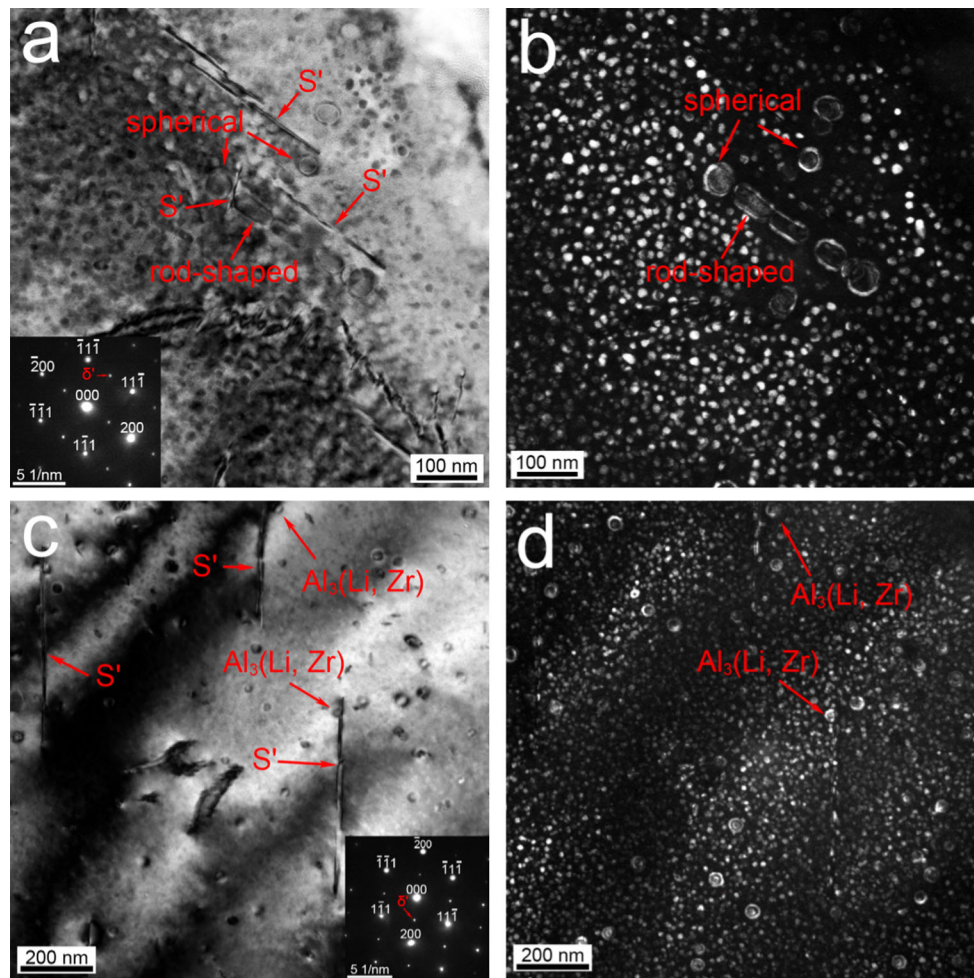


Figure 10 TEM images of the 1 Mg and 1.5 Mg alloys aged at 175 °C for 8 h: **a** and **b** BF and δ' CDF images of 1 Mg alloy showing the preferential nucleation of S' phases in the vicinity of $\text{Al}_3(\text{Li}, \text{Zr})$ precipitates with spherical- and rod-shaped

morphology ($\mathbf{B} = [011]$); **c** and **d** BF and δ' CDF images of 1.5 Mg alloy showing the homogeneous distribution of δ' particles and the similar interactions between S' phases and $\text{Al}_3(\text{Li}, \text{Zr})$ precipitates ($\mathbf{B} = [011]$).

resulted in the formation of spherical δ' caps [36, 41]. The other is the interaction of S' with $\text{Al}_3(\text{Li}, \text{Zr})$ composite precipitates. As exemplified in Fig. 10a and b, the lath-shaped S' phases are observed to preferentially nucleate in the vicinity of the $\text{Al}_3(\text{Li}, \text{Zr})$ particles with spherical- and/or rod-shaped morphology in the 1 Mg alloy. Similar interactions between S' and $\text{Al}_3(\text{Li}, \text{Zr})$ precipitates are also observed in the 1.5 Mg alloy as illustrated in Fig. 10c and d. The number density of S' phase is frequently higher in the vicinity of $\text{Al}_3(\text{Li}, \text{Zr})$ precipitates, contributing to the enhancement of tensile ductility. However, the coarsening of S' phases distributed in uneven manner will neutralize this ductility improvement.

The PA stage microstructures

Based on the ageing hardening curves shown in Fig. 6, the addition of Mg shortened the time required to reach the peak hardness from 128 h (base alloy) to 32 h (0.5 Mg alloy). For clarity, microstructures of the selected alloys aged for 32 h and 128 h are selected for the PA microstructure observations.

Figure 11a and b is, respectively, BF and δ' CDF images of the base alloy aged for 32 h at 175 °C ($\mathbf{B} = [011]$). The mean size of δ' particles is significantly increased from about 14.8 nm to 28.0 nm with the ageing time prolonged from 8 h to 32 h. Concurrently, δ' phases are observed to nucleate on the coherent, broad faces of θ' phases, resulting in the

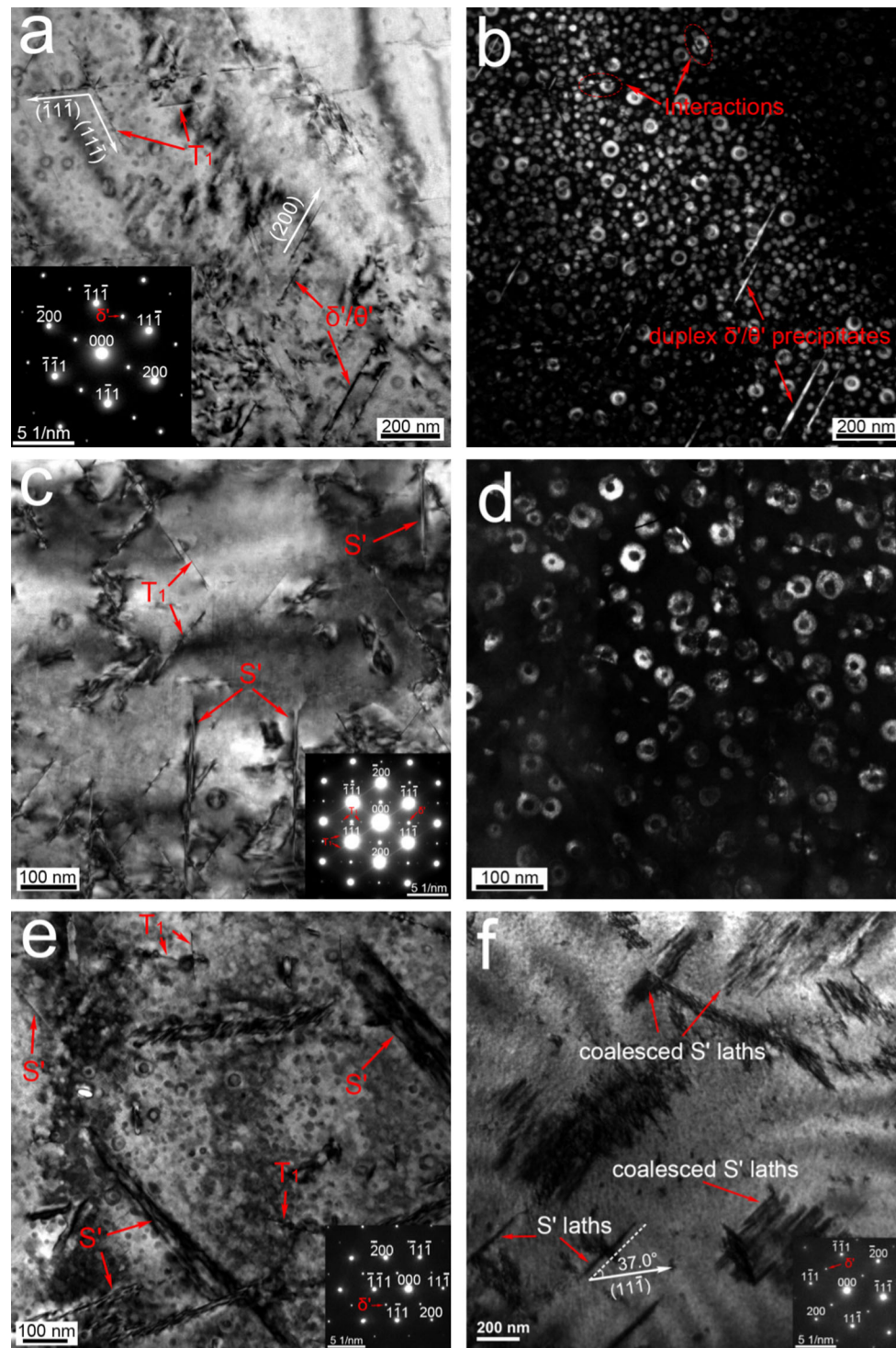


Figure 11 TEM images of studied alloys aged at 175 °C for 32 h: **a** the BF image of the base alloy ($\mathbf{B} = [011]$, inset), showing the lengthening of edge-on T_1 and θ' precipitates; **b** the δ' CDF image corresponding to **(a)**, recorded using 110 superlattice reflections, indicating the coarsening of δ' and development of duplex δ'/θ' precipitates; **c** and **d** BF and δ' CDF images of 0.5 Mg alloy

illustrating the increased T_1 and S' and development of $Al_3(Li, Zr)$ particles ($\mathbf{B} = [011]$); **e** the BF image of the 1 Mg alloy ($\mathbf{B} = [011]$, inset), showing the presence of sparse T_1 plates and obvious coarsening S' phases; **f** the BF image of the 1.5 Mg alloy illustrating the dramatic coalescence of uneven S' laths and the absence of T_1 plates ($\mathbf{B} = [011]$, inset).

formation of “plate-like” duplex δ'/θ' precipitates (illustrated in Fig. 11b). The amount of plate-like T_1 and lath-shaped S' phases is increased in 0.5 Mg alloy after ageing for 32 h at 175 °C as evidenced by the BF image viewed along $[110]_\alpha$ zone axis shown in Fig. 11c. As illustrated by the SAED inset in Fig. 11c, the presence of T_1 phases can also be confirmed by the two sets of reflections distributed around the 110 type superlattice reflections combined with the streaks in the $\langle 1\bar{1}1 \rangle$ directions, which is fully consistent with previous published works [11, 42]. Figure 11e is a BF image of 1 Mg alloy, indicating the obvious coarsening of S' laths and sparse T_1 plates. It can be concluded that the precipitation of T_1 phases was retarded with the Mg content increased from 0.5 to 1%. Moreover, the increased S' precipitates coalesce to form coarse laths distributed in uneven manner observed in the 1.5 Mg alloy (presented in Fig. 11e and f). Thus, it can be summarized that minor Mg addition would result in the formation of fine S' laths instead of plate-like θ' phases. The balance of S' and T_1 competitive precipitation depends critically on the relative Mg content. The precipitation of T_1 would be strongly delayed or retarded when the Mg content exceeds 1%, resulting in the predominance of S' and δ' phases in 1 Mg and 1.5 Mg alloy. Moreover, the addition of Mg is supposed to retard the coarsening of δ' since the average δ' particle size of Mg-added alloys is smaller than that in the base alloy at the same ageing time.

Figure 12a through 12f shows comparative microstructures of the base and 0.5 Mg alloys aged for 128 h at 175 °C. PA microstructures of the base alloy, as illustrated in Fig. 12b and c, consist of edge-on T_1 plates lying on $(1\bar{1}1)$ plane with a large aspect ratio, duplex δ'/θ' precipitates and a few face-on T_1 variant (arrowed A in Fig. 12b showing T_1 variant orientated with broad face inclined to the beam direction). The long vertical streaks shown in Fig. 12a are originated from the T_1 plates lying on $(1\bar{1}1)$ plane. In addition to the typical T_1/δ' interactions (marked A in Fig. 12c), T_1 plates gradually lengthen and cut/grow through the duplex δ'/θ' precipitates (marked B in Fig. 12c), resulting in an offset in the δ' coating (or shell). Tosten et al. [41] attributed this phenomenon to the Li diffusion to diminish the imbalance in surface tension forces at the $T_1/\delta'/\alpha$ triple junctions. In contrast, the additional streaks in the (402) and $(0\bar{4}2)$ directions showed in the SAED pattern of 0.5 Mg alloy (marked by dotted

oval in Fig. 12d) confirm the presence of S' laths. Denser distribution of edge-on and face-on T_1 plates (indicated by dotted oval A in Fig. 12e) is observed in the 0.5 Mg alloy accompanied by the coarsening of S' and gradual dissolution of δ' particles (presented in Fig. 12f).

The OA stage microstructures

Continued ageing leads to the significant lengthening of T_1 plates and duplex δ'/θ' precipitates in the base alloy accompanied by gradual dissolution of δ' presented in Fig. 13b. The δ' CDF image illustrates that the thermal stability of T_1 plates, duplex δ'/θ' precipitates and $Al_3(Li, Zr)$ composite precipitates is superior to that of δ' . The coarsening of these phases was believed to continue at the expense of gradual δ' dissolution. Figure 13c is a T_1 CDF image of the base alloy aged for 600 h, demonstrating the presence of a higher number density of T_1 plates lying on $(1\bar{1}1)$ plane with greatly improved aspect ratio. (The aspect ratio for a particular particle is defined by taking the ratio of the maximum to the minimum dimension.) The OA base alloy is characterized by predominant T_1 plates, duplex δ'/θ' and $Al_3(Li, Zr)$ precipitates. Similarly, severer interactions between the T_1 plates and δ' (marked A) and the duplex δ'/θ' precipitates (marked B) in the base alloy are also observed (shown in Fig. 13b). Figure 13d is a BF image of the 0.5 Mg alloy (viewed along the $[110]_\alpha$ zone axis) showing the presence of two edge-on T_1 variants with smaller aspect ratio and sparse S' phases. The lengthening rate of T_1 phases in the 0.5 Mg alloy is lower than that in the base alloy, which is possibly attributed to the retarded coarsening rate of δ' and competitive precipitation with S' phases.

A summary of the phases observed in all studied alloys during ageing is provided in Table 3. The addition of Mg would produce significant influence on the ageing precipitation behavior. Minor Mg addition (0.5%) encourages the precipitation of S' instead of the θ' plates. The increased Mg content ($\geq 1\%$) appears to exert a significant influence on the competitive precipitation of S' and T_1 phases. Increasing the amount of Mg promotes the precipitation of S' at the expense of T_1 phases, resulting in the retarded T_1 precipitation and lower strength. S' and δ' phases are the predominant strengthening phases in alloys with relatively high Mg content ($> 1\%$), and T_1 phase is failed to be observed in aged

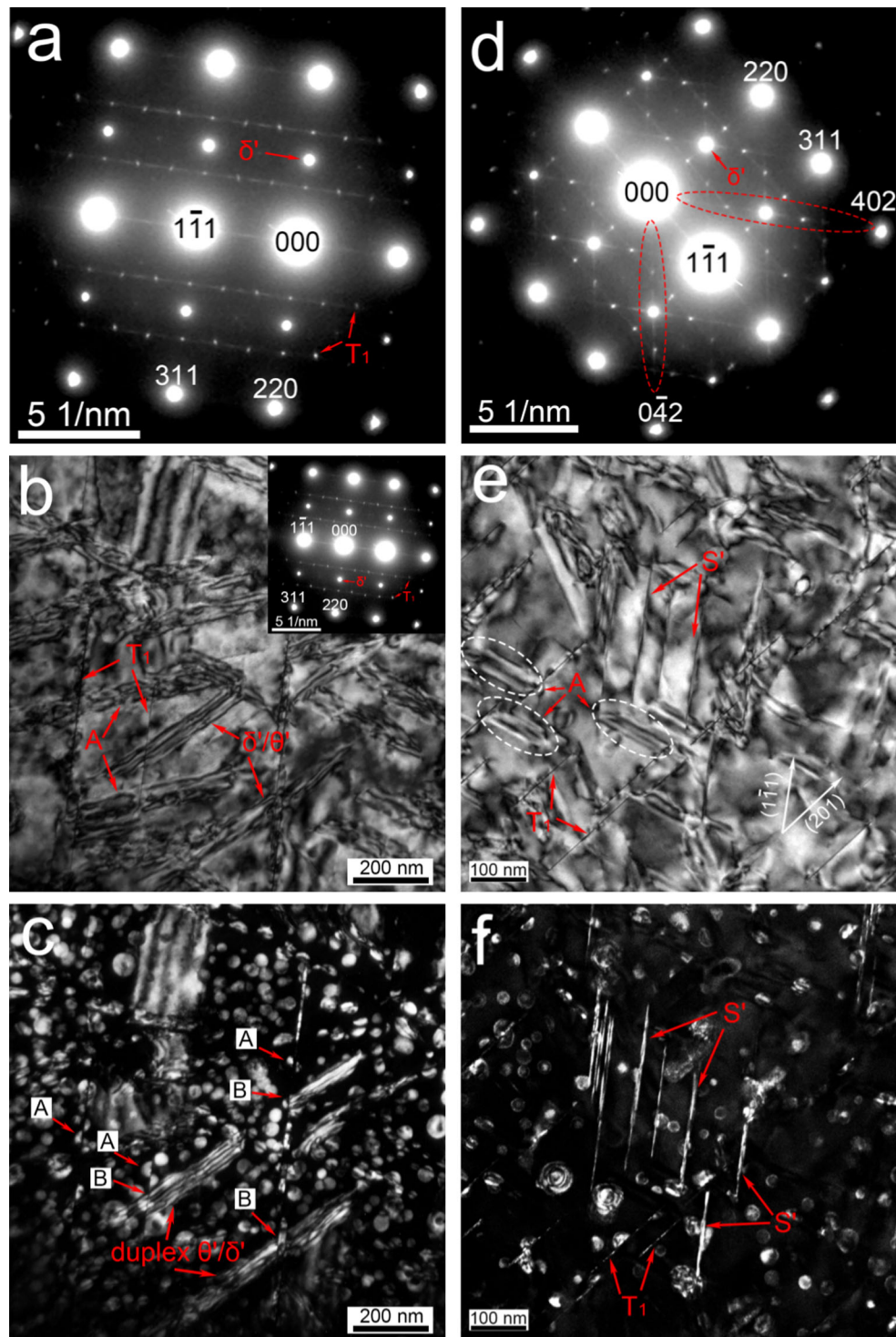


Figure 12 TEM images of the base and 0.5 Mg alloys aged at 175 °C for 128 h: **a** SAED for the base alloy ($\mathbf{B} = [\bar{1}12]$); **b** BF image of PA base alloy showing the δ'/θ' precipitates, edge-on T_1 plates and face-on T_1 variant (arrowed A); **c** the δ' CDF image corresponding to (**b**), illustrating numerous interactions between the T_1 plates and δ' (marked A) and the duplex θ'/δ' precipitates

(marked B); **d** SAED for the 0.5 Mg alloy ($\mathbf{B} = [\bar{1}12]$), showing additional streaks in the $\langle 420 \rangle$ directions (indicated by dotted oval); **e** BF image of the OA 0.5 Mg alloy showing S' laths, T_1 plates and face-on T_1 variant (indicated by dotted oval A); **f** the δ' CDF image corresponding to (**e**) showing the presence of S' laths, T_1 plates and δ' dissolution.

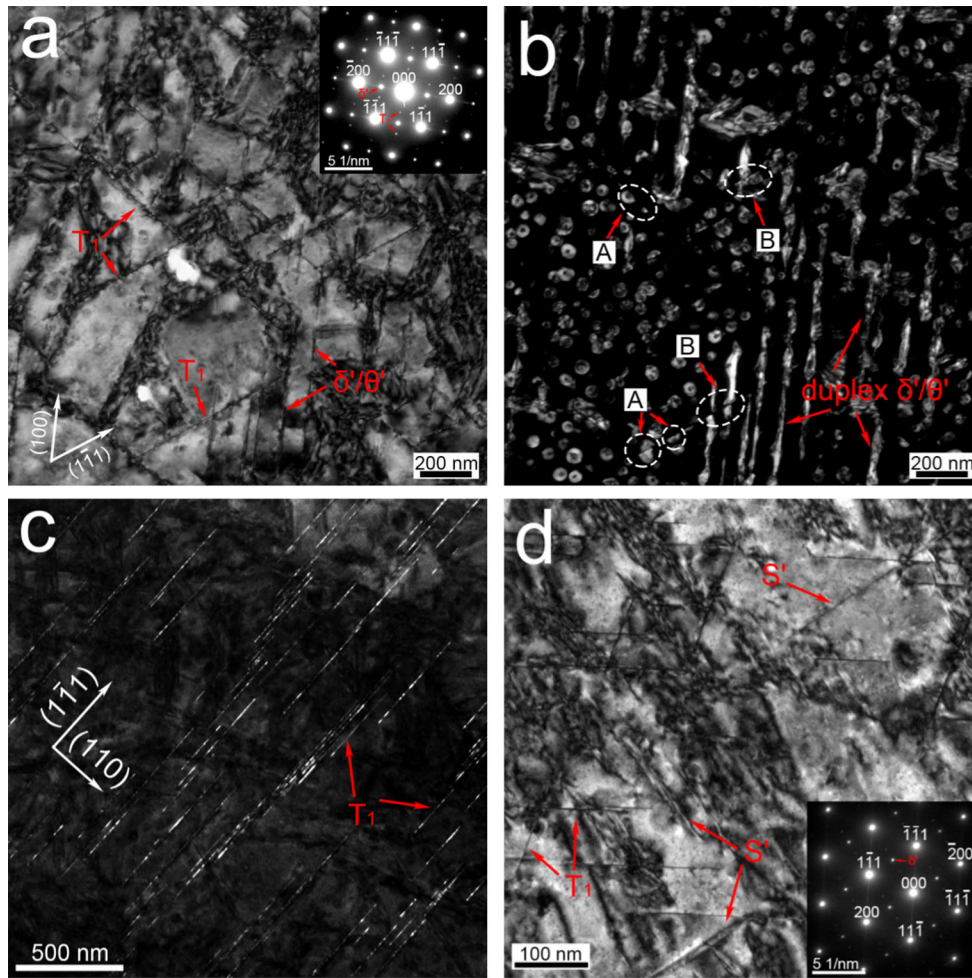


Figure 13 TEM images of the OA base and 0.5 Mg alloys aged at 175 °C for 600 h: **a** and **b** BF and corresponding δ' CDF image of the base alloy showing the δ' dissolution and severe interactions between the T_1 plates and δ' (marked A) and the duplex δ'/θ' precipitates (marked B); **c** T_1 CDF image of the base alloy aged for

600 h showing T_1 variant on $(1\bar{1}1)$ plane with large aspect ratio ($g = \frac{1}{2}(1\bar{1}1)$), matrix orientation $B = [\bar{1}12]$; **d** BF image of the 0.5 Mg alloy showing inhomogeneous distribution of S' and T_1 phases ($B = [011]$, inset).

1.5 Mg alloy. However, the increased S' phases tend to distribute in a sparse and uneven manner, resulting in the formation of coarse laths. The homogeneous precipitation of S' phases depends critically on the combination of Cu and Mg supersaturation and

free vacancy (or heterogeneous nucleation sites) [33]. This work suggests that it is not feasible to promote the homogeneous precipitation of S' phases via increasing the addition of Mg for cast Al–Li–Cu alloys. The improved precipitation of S' phases

Table 3 Precipitates present at different ageing conditions

Condition	Precipitates after ageing at 175 °C			
	Base alloy	0.5 Mg alloy	1 Mg alloy	1.5 Mg alloy
As-quenched	δ', β'	δ', β'	δ', β'	δ', β'
Under-aged	$\delta', \delta'/\beta', \theta', T_1$	$\delta', \delta'/\beta', S', T_1$	$\delta', \delta'/\beta', S'$	$\delta', \delta'/\beta', S'$
Peak-aged	$\delta', \delta'/\beta', \delta'/\theta', T_1$	$\delta', \delta'/\beta', S', T_1$	$\delta', \delta'/\beta', S', T_1$	$\delta', \delta'/\beta', S'$
Over-aged	$\delta'/\beta', \delta', T_1, \delta'/\theta'$	$\delta'/\beta', \delta', S', T_1$	$\delta', \delta'/\beta', S', T_1$	$\delta', \delta'/\beta', S'$

The main precipitates are indicated in bold type, and the δ'/β' refers to the core/shell $Al_3(Li, Zr)$ composite precipitates

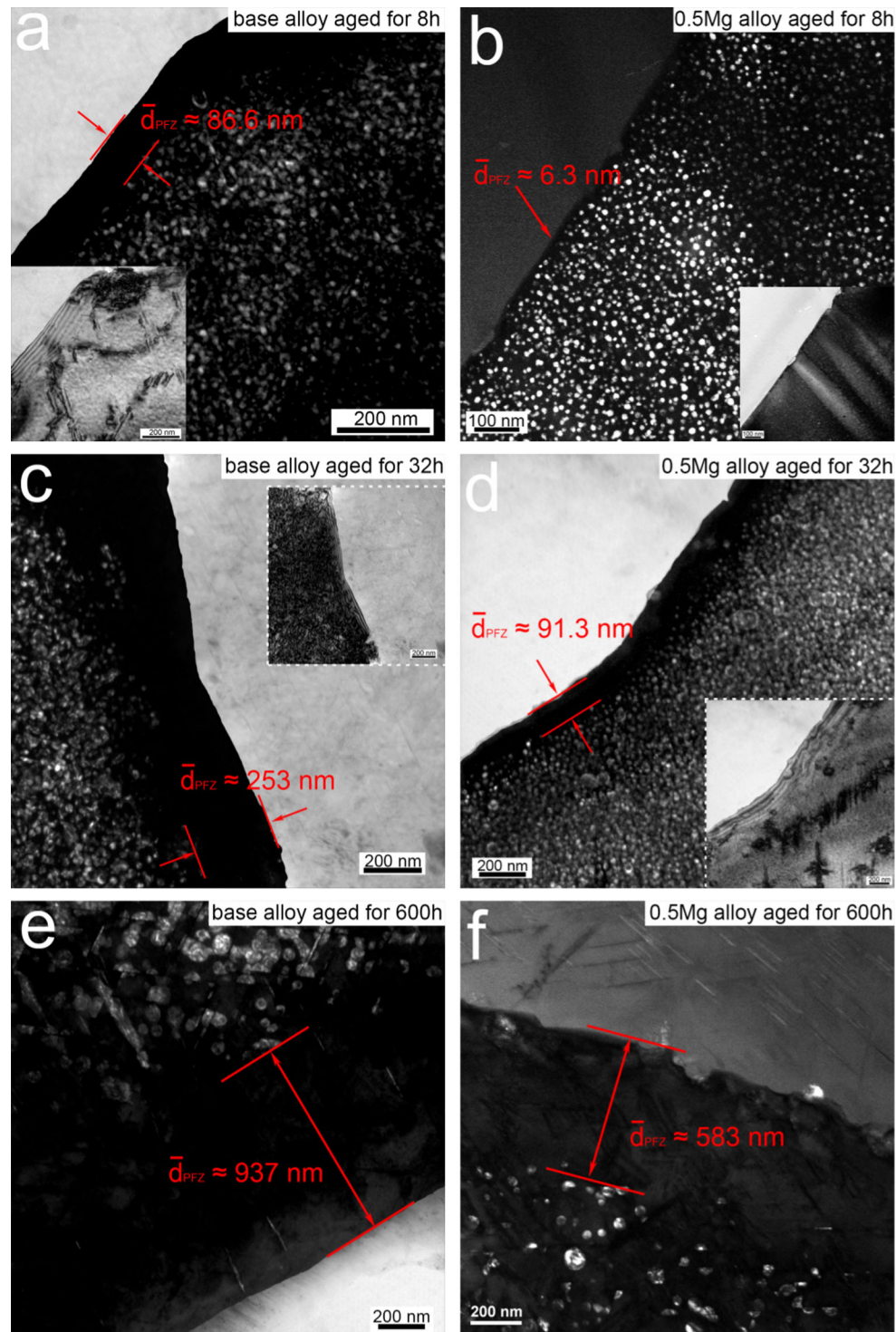


Figure 14 Development of δ' -precipitation-free zones (δ' -PFZs) half width as a function of ageing time in the base and 0.5 Mg alloys: **a** δ' CDF image of the base alloy aged for 8 h taken near the grain boundary (corresponding BF image inset), indicating the presence of δ' -precipitate-free zones (δ' -PFZs); **b** δ' CDF image of the 0.5 Mg alloy aged for 8 h taken near the grain boundary

(corresponding BF image inset); **c** and **d** the δ' CDF images of the base and 0.5 Mg alloys aged for 32 h, respectively, showing obvious widening of δ' -PFZs (corresponding BF images for each alloy inset); **e** and **f** the δ' CDF images of the base and 0.5 Mg alloys aged for 600 h, respectively, showing the well-developed δ' -PFZs in over-aged state.

frequently coalesces to form coarse clusters of S' laths, possibly attributed to the intrinsically low density of heterogeneous nucleation sites as compared to that of the wrought alloys. T_1 and $Al_3(Li, Zr)$ composite precipitates (also denoted by δ'/β') exhibit higher coarsening resistance (or thermal stability) as evidenced by the OA microstructures. However, the T_2 phases are failed to be identified in all aged samples. The best balance of S' and T_1 competitive precipitation is obtained in 0.5 Mg alloy, which possess the best combination of strength and ductility.

Effect of Mg content on the development of δ' -precipitation-free zones

Figure 14 presents comparative micrographs showing the development of δ' -precipitate-free zones (δ' -PFZs) as a function of ageing time in the base and 0.5 Mg alloys. All the δ' -PFZs half widths are measured from the grain boundary to the nearest δ' particles from the edge of δ' -PFZs. There exist no δ' -PFZs in the as-quenched studied alloys based on the TEM observations. There occur significantly systematic increases in the average δ' -PFZs half widths with the increasing ageing time for both alloys, accompanied by the continued coarsening and gradual dissolution of δ' phases. The growth of δ' -PFZs adjacent to the grain boundaries is slower in the 0.5 Mg alloy as evidenced by comparing the δ' -PFZs half widths at the same ageing time for the two alloys (presented in Fig. 14).

The fracture process of Al–Li alloys is reported to be governed by several concurrent and mutually competitive factors involving the planar slip, δ' -PFZs, grain boundary precipitates and grain boundary segregations (including Li, hydrogen and alkali-metal impurities) [43–45]. Grain boundary equilibrium δ (AlLi) phases are failed to be identified in this work. The monotonic reduction in ductility observed with the increase in ageing time is largely attributed to the planar slip associated with δ' phases and the growth of δ' -PFZs. Jha and Sanders et al. [46] demonstrated that the growth of δ' -PFZs could be interpreted as a diffusion-controlled process, which was assumed to follow a parabolic growth law expressed by:

$$h = K_p t^{1/2} \quad (5)$$

where h is the δ' -PFZs half width, t is the ageing time at a given temperature and K_p is the δ' -PFZs growth rate constant. The measured δ' -PFZs half widths as a function of ageing time for the base and 0.5 Mg alloys

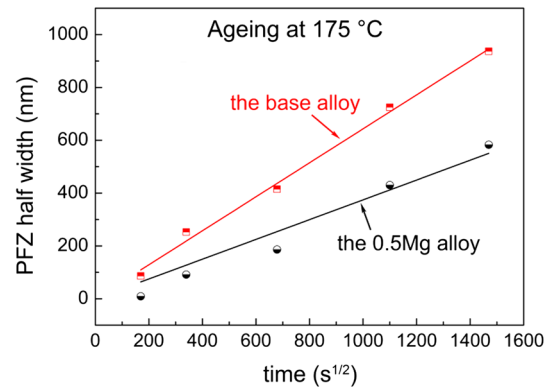


Figure 15 Measured δ' -PFZs half widths in the base and 0.5 Mg alloys plotted as a function of square root of the ageing time at 175 °C. The linear regression lines have been evaluated taking the intercept term as zero.

are displayed in Fig. 15. The K_p for the base and 0.5 Mg alloys, evaluated using linear regression analysis with the intercept term taken as zero, are $0.64 \text{ nm}\cdot\text{s}^{1/2}$ and $0.37 \text{ nm}\cdot\text{s}^{1/2}$, respectively. It is evident that the δ' -PFZs growth rate constant in the 0.5 Mg alloy is lower than that in the base alloy, which could be explained as follows. Owing to the relatively high Mg–vacancy binding energy ($0.25 \pm 0.03 \text{ eV}$) reported [47], the growth of δ' and δ' -PFZs during ageing would be consequently retarded in the presence of Mg. Hiro-sawa et al. [48] also demonstrated that the addition of Mg lowered the growth rate of δ' particles, which is consistent with this work. The detailed investigations dedicated to the influence of Mg addition on the growth rate of δ' particles and δ' -PFZs will be the subject of our subsequent research.

Conclusions

The influences of Mg content on the microstructures and mechanical properties of cast Al–2Li–2Cu–0.2Zr alloy were investigated. The major findings of this work can be summarized as follows:

1. Increasing amount of Mg progressively refines the grain structure of as-cast base alloy accompanied by the increased volume fraction of secondary phases.
2. Numerous precipitate interactions occur in the base alloy between the T_1 and δ' and duplex δ'/θ' precipitates. The S' phase could preferentially nucleate in the vicinity of $Al_3(Li, Zr)$ precipitates with faceted or rod-shaped morphology.

3. The formation of θ' would be almost suppressed, and S' phases are consequently introduced due to the addition of Mg. Increasing the amount of Mg promotes the precipitation of S' at the expense of T_1 phases, resulting in the predominance of S' in the 1 Mg and 1.5 Mg alloys.
4. The improved precipitation of S' phase tends to coalesce to form coarse laths distributed in uneven clusters for the lack of heterogeneous nucleation sites, which exerts deleterious influence on the alloy strength and ductility.
5. Addition of Mg could lower the growth rate of δ' particle and δ' -PFZs as a result of the high Mg-vacancy binding energy.
6. The optimal Mg addition in cast Al–2Li–2Cu–0.2Zr alloy should be 0.5%.

Appendix

A detailed illustration of the identification of the main strengthening phases based on the TEM techniques is available in the supplementary file attached.

Acknowledgements

This work was supported by the National Key R&D Program of China (Grant No. 2016YFB0301003) and the 111 Project (Grant No. B16032).

Compliance with ethical standards

Conflict of interest The authors declare that they have no conflict of interest.

Ethical standards This article does not contain any studies with human or animal subjects.

Electronic supplementary material: The online version of this article (<https://doi.org/10.1007/s10853-018-2826-y>) contains supplementary material, which is available to authorized users.

References

- [1] Starke EA Jr, Sanders TH, Palmer IG (1981) New approaches to alloy development in the Al–Li system. *JOM* 33:24–33
- [2] Rioja RJ, Liu J (2012) The evolution of Al–Li base products for aerospace and space applications. *Metall Mater Trans A* 43:3325–3337
- [3] Abd El-Aty A, Xu Y, Guo X, Zhang S-H, Ma Y, Chen D (2018) Strengthening mechanisms, deformation behavior, and anisotropic mechanical properties of Al–Li alloys: a review. *J Adv Res* 10:49–67
- [4] Gilmore DL, Starke EA Jr (1997) Trace element effects on precipitation processes and mechanical properties in an Al–Cu–Li alloy. *Metall Mater Trans A* 28:1399–1415
- [5] Csontos AA, Starke EA Jr (2000) The effect of processing and microstructure development on the slip and fracture behavior of the 2.1 wt pct Li AF/C-489 and 1.8 wt pct Li AF/C-458 Al–Li–Cu–X alloys. *Metall Mater Trans A* 31:1965–1976
- [6] Gumbmann E, De Geuser F, Sigli C, Deschamps A (2017) Influence of Mg, Ag and Zn minor solute additions on the precipitation kinetics and strengthening of an Al–Cu–Li alloy. *Acta Mater* 133:172–185
- [7] Gable BM, Zhu AW, Csontos AA, Starke EA Jr (2001) The role of plastic deformation on the competitive microstructural evolution and mechanical properties of a novel Al–Li–Cu–X alloy. *J Light Metals* 1:1–14
- [8] Noble B, Thompson GE (1971) Precipitation characteristics of aluminium–lithium alloys. *Metal Sci J* 5:114–120
- [9] Silcock JM (1959–1960) The structural ageing characteristics of Al–Cu–Li alloys. *J Inst Metals* 88:357–364
- [10] Silcock JM, Heal TJ, Hardy HK (1954) Structural ageing characteristics of binary aluminium–copper alloys. *J Inst Metals* 82:239–248
- [11] Huang JC, Ardell AJ (1987) Crystal structure and stability of T_1 precipitates in aged Al–Li–Cu alloys. *Mater Sci Technol* 3:176–188
- [12] Ratchev P, Verlinden B, De Smet P, Van Houtte P (1998) Precipitation hardening of an Al–4.2 wt% Mg–0.6 wt% Cu alloy. *Acta Mater* 46:3523–3533
- [13] Gupta AK, Gaunt P, Chaturvedi MC (1987) The crystallography and morphology of the S' -phase precipitate in an Al (CuMg) alloy. *Philos Mag A* 55:375–387
- [14] Srinivasan S, Desch PB, Schwarz RB (1991) Metastable phases in the Al_3X ($X = Ti, Zr, \text{ and } Hf$) intermetallic system. *Scri Metall Mater* 25:2513–2516
- [15] Kang S, Grant NJ (1987) Rapidly solidified P/M X2020 aluminum alloys. *Metall Trans A* 18:2037–2046
- [16] Ball MD, Lloyd DJ (1985) Particles apparently exhibiting five-fold symmetry in Al–Li–Cu–Mg alloys. *Scr Metall* 19:1065–1068
- [17] Gumbmann E, Lefebvre W, De Geuser F, Sigli C, Deschamps A (2016) The effect of minor solute additions on the precipitation path of an Al–Cu–Li alloy. *Acta Mater* 115:104–114

- [18] Kumar KS, Heubbaum FH (1997) The effect of Li content on the natural aging response of Al–Cu–Li–Mg–Ag–Zr alloys. *Acta Mater* 45:2317–2327
- [19] Kim JD, Park JK (1993) Effect of stretching on the precipitation kinetics of an Al–2.0Li–2.8Cu–0.5Mg(–0.13Zr) alloy. *Metall Trans A* 24:2613–2621
- [20] Tsvoulas D, Prangnell PB (2014) The effect of Mn and Zr dispersoid-forming additions on recrystallization resistance in Al–Cu–Li AA2198 sheet. *Acta Mater* 77:1–16
- [21] Chen A, Zhang L, Wu G, Sun M, Liu W (2017) Influences of Mn content on the microstructures and mechanical properties of cast Al–3Li–2Cu–0.2Zr alloy. *J Alloys Compd* 715:421–431
- [22] Chen A, Wu G, Zhang L, Zhang X, Shi C, Li Y (2016) Microstructural characteristics and mechanical properties of cast Al–3Li–xCu–0.2Zr alloy. *Mater Sci Eng A* 677:29–40
- [23] Chen A, Peng Y, Zhang L, Wu G, Li Y (2016) Microstructural evolution and mechanical properties of cast Al–3Li–1.5Cu–0.2Zr alloy during heat treatment. *Mater Charact* 114:234–242
- [24] Zhang X, Zhang L, Wu G, Liu W, Shi C, Tao J, Sun J (2017) Microstructural evolution and mechanical properties of cast Al–2Li–2Cu–0.5Mg–0.2Zr alloy during heat treatment. *Mater Charact* 132:312–319
- [25] Mukhopadhyay AK, Zhou DS, Yang QB (1992) Effect of variation in the Cu: Mg ratios on the formation of T2 and C phases in AA 8090 alloys. *Scri Metall Mater* 26:237–242
- [26] Fridlyander IN, Rokhlin LL, Dobatkina TV, Nikitina NI (1993) Investigation of the phase equilibria in aluminum alloys containing lithium. *Met Sci Heat Treat* 35:567–571
- [27] Wang F, Liu Z, Qiu D, Taylor JA, Easton MA, Zhang M-X (2013) Revisiting the role of peritectics in grain refinement of Al alloys. *Acta Mater* 61:360–370
- [28] Liu YL, Hu ZQ, Zhang Y, Shi CX (1993) The solidification behavior of 8090 Al–Li alloy. *Metall Trans B* 24:857–865
- [29] Hekmat-Ardakan A, Elgallad EM, Ajersch F, Chen XG (2012) Microstructural evolution and mechanical properties of as-cast and T6-treated AA2195 DC cast alloy. *Mater Sci Eng A* 558:76–81
- [30] Dorward RC (1988) Solidus and solvus isotherms for quaternary Al–Li–Cu–Mg alloys. *Metall Trans A* 19:1631–1634
- [31] Gayle FW, Vander Sande JB (1984) “Composite” precipitates in an Al–Li–Zr alloy. *Scr Metall* 18:473–478
- [32] Gayle FW, Heubbaum FH, Pickens JR (1990) Structure and properties during aging of an ultra-high strength Al–Cu–Li–Ag–Mg alloy. *Scr Metall Mater* 24:79–84
- [33] Gregson PJ, Flower HM, Tite CNJ, Mukhopadhyay AK (1986) Role of vacancies in coprecipitation of δ' - and S-phases in Al–Li–Cu–Mg alloys. *Mater Sci Technol* 2:349–353
- [34] Baumann SF, Williams DB (1985) Experimental observations on the nucleation and growth of δ' (Al₃Li) in dilute Al–Li alloys. *Metall Trans A* 16:1203–1211
- [35] Gleiter H, Hornbogen E (1965) Theorie der Wechselwirkung von Versetzungen mit kohärenten geordneten Zonen (I). *Phys Status Solidi* 12:235–250
- [36] Flower HM, Gregson PJ (1987) Solid state phase transformations in aluminium alloys containing lithium. *Mater Sci Technol* 3:81–90
- [37] Satya Prasad K, Gokhale AA, Mukhopadhyay AK, Banerjee D, Goel DB (1999) On the formation of faceted Al₃Zr (β') precipitates in Al–Li–Cu–Mg–Zr alloys. *Acta Mater* 47:2581–2592
- [38] Tsvoulas D, Robson JD (2015) Heterogeneous Zr solute segregation and Al₃Zr dispersoid distributions in Al–Cu–Li alloys. *Acta Mater* 93:73–86
- [39] Gregson PJ, Flower HM (1985) Microstructural control of toughness in aluminium–lithium alloys. *Acta Metall* 33:527–537
- [40] Balducci E, Ceschini L, Messieri S, Wenner S, Holmestad R (2017) Thermal stability of the lightweight 2099 Al–Cu–Li alloy: tensile tests and microstructural investigations after overaging. *Mater Des* 119:54–64
- [41] Tosten MH, VasudÉvan AK, Howell PR (1988) The aging characteristics of an Al-2 Pct Li-3 Pct Cu-0.12 Pct Zr alloy at 190 °C. *Metall Trans A* 19:51–66
- [42] Noble B, Thompson GE (1972) T₁ (Al₂CuLi) precipitation in aluminium–copper–lithium alloys. *Metal Sci J* 6:167–174
- [43] Lynch SP, Muddle BC, Pasang T (2001) Ductile-to-brittle fracture transitions in 8090 Al–Li alloys. *Acta Mater* 49:2863–2874
- [44] Goswami R, Bernstein N (2015) Effect of interfaces of grain boundary Al₂CuLi plates on fracture behavior of Al–3Cu–2Li. *Acta Mater* 87:399–410
- [45] Suresh S, Vasudevan AK, Tosten M, Howell PR (1987) Microscopic and macroscopic aspects of fracture in lithium-containing aluminum alloys. *Acta Metall* 35:25–46
- [46] Jha S, Sanders T, Dayananda M (1987) Grain boundary precipitate free zones in Al–Li alloys. *Acta Metall* 35:473–482
- [47] Beatrice CRS, Garlipp W, Cilense M, Adorno AT (1995) Vacancy-Mg atom binding energy in Al–Mg alloys. *Scr Metall Mater* 32:23–26
- [48] Hirosawa S, Sato T, Kamio A (1998) Effects of Mg addition on the kinetics of low-temperature precipitation in Al–Li–Cu–Ag–Zr alloys. *Mater Sci Eng A* 242:195–201